Comparison of space radiation GCR models to AMS heavy ion data

Kathryn Whitman[a,*], John W. Norbury[b], Kerry Lee[c], Tony C. Slaba[b],
Francis F. Badavi[d]

[a]*University of Houston, Houston, Texas 77204, USA*
[b]*NASA Langley Research Center, Hampton, Virginia 23681, USA*
[c]*NASA Johnson Space Center, Houston, Texas 77058, USA*
[d]*Old Dominion University, Norfolk, Virginia 23529, USA*

Abstract

Galactic cosmic rays (GCR) are a constant source of radiation that constitutes one of the major hazards during deep space exploration missions for both astronauts and hardware. In this work, GCR models commonly used by the space radiation protection community are compared with recently published high-precision, high-resolution measurements of cosmic ray lithium, beryllium, boron, carbon, nitrogen, and oxygen fluxes along with their ratios (Li/B, Li/C, Li/O, Be/B, Be/C, Be/O, B/C, B/O, C/O, N/B, N/O) from the Alpha Magnetic Spectrometer (AMS). All of the models were developed and calibrated prior to the publication of this AMS data, therefore this is an opportunity to validate the models against an independent data set. This paper is a compliment to the previously published comparison of GCR models with AMS hydrogen, helium, and the boron-to-carbon ratio (Norbury et al., 2018).

Keywords: Space radiation, Galactic cosmic rays, Alpha Magnetic Spectrometer

1. Introduction

Galactic cosmic rays (GCR) are a continuous source of background radiation with significant consequences for human exploration missions outside low Earth orbit. Hydrogen and helium make up the majority of cosmic rays, but heavy ions of lithium

---

[*]Corresponding author.
Email address: kathryn.whitman@nasa.gov (Kathryn Whitman)

up to iron and nickel do make up an important component of the space radiation environment. A series of sensitivity studies investigated the contribution of different GCR species to effective dose behind shielding (Slaba and Blattnig, 2014a,b; Slaba et al., 2014). In the case of 20 g/cm^2 aluminum shielding, these studies found that heavy ions with Z $\geq$ 3 contributed nearly 30% of the total effective dose, most of which was attributed to ions with energies between 0.5 - 4 GeV/n (Slaba and Blattnig, 2014a). Clearly, it is important to know the particle spectrum in this energy range, however high precision, high energy resolution measurements of heavy ion GCR have been limited. Recently, high precision cosmic ray spectra measured by the Alpha Magnetic Spectrometer (AMS), which is operating on the International Space Station (ISS), were published for lithium, beryllium, boron, carbon, nitrogen, and oxygen along with their ratios (Li/B, Li/C, Li/O, Be/B, Be/C, Be/O, B/C, B/O, C/O, N/B, N/O) for ∼0.4 GeV/n to a few TeV/n (Aguilar et al., 2017, 2018a,b). All of the ion fluxes were integrated over a 5-year period from May 19, 2011 to May 26, 2016.

This paper continues a series which compares the galactic cosmic ray (GCR) models used by the NASA, ROSCOSMOS and the European Space Agency (ESA) to recently published measurements from AMS. NASA employs the Badhwar-O'Neill model (BON2014) (O'Neill et al., 2015); ROSCOSMOS recently developed the new Skobeltsyn Institute of Nuclear Physics (SINP) model (Kuznetsov et al., 2017), and the ESA tool is the Deutsches zentrum für Luft- und Raumfahrt (DLR) model (Matthia et al., 2013). In a prior paper, these models were compared with AMS hydrogen, helium, and boron-to-carbon measurements (Norbury et al., 2018). In this paper, the comparison is extended to the recently published AMS heavy ion fluxes from lithium to oxygen and their ratios.

2. Primary and Secondary Cosmic Rays

When galactic cosmic ray abundances are compared with abundances of elements in the solar system, it becomes clear that there are different types of GCR populations. Some GCR ions, such as C, N, and O, have relative abundances similar to the solar system, whereas other GCR ions, such as Li, Be, and B, are different by orders of magnitude, shown in Figure 1. These populations arise from different production mechanisms. Much of C, N, and O are produced in stars via the CNO cycle and then accelerated in energetic processes, such as supernovae, to high energies (Henry et al., 2000). For this reason, they have similar relative abundances to the solar system. Li, Be, and B are fragile nuclei that are destroyed in stellar interiors (Vangioni-Flam et al., 2000), making them very rare in the material that makes up the solar system;
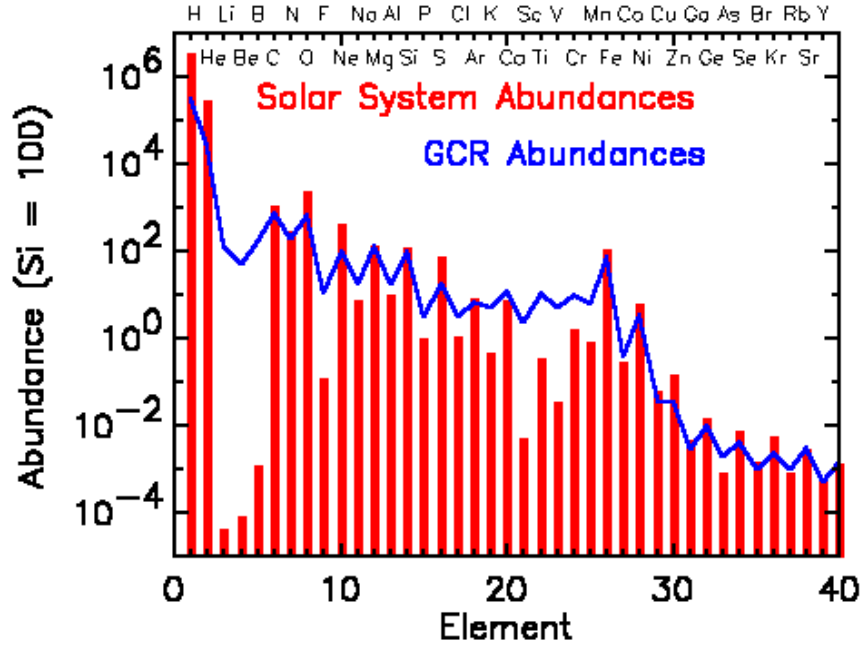
Figure 1: Elemental abundances relative to silicon in the solar system are shown in red and GCR abundances relative to GCR silicon are shown in blue. Li, Be, and B are more abundant in the GCR population compared to the solar system, whereas C, N, and O show similar abundances. Image credit: NASA (https://imagine.gsfc.nasa.gov/science/toolbox/cosmic_rays2_orig.html)

however, they are produced as secondary GCR when heavier primary GCR nuclei interact with interstellar matter (Vangioni-Flam et al., 2000; Strong et al., 2007) resulting in much larger abundances than observed in the solar system. The full physics explanation of each of the GCR abundances is more complex, with each ion having both primary and secondary sources, but the production mechanisms described here are thought to play the most significant roles in classifying each ion as a primary- or secondary-type GCR. Nitrogen and Boron are somewhat special cases: N has significant primary *and* secondary components, while B is believed to be produced almost purely as secondary nuclei (Aguilar et al. (2018b) and references therein).

C, O, N and Li, Be, B are different populations of GCRs produced by different mechanisms, thus they have very different spectral shapes, as demonstrated in Figure 2. The AMS spectrum for each heavy ion has been rescaled by kinetic energy (KE) raised to the power of 2.7 ($KE^{2.7}$) to highlight the shape of the spectrum at high energies. An additional scaling factor is applied (shown in the legend and equiva-

3

lent to the flux ∼8 GeV/n) so that the fluxes could be compared on a similar scale. Secondary cosmic rays Li (dark blue), Be (blue), and B (turquoise) show a characteristic downturn in the slope above ∼20 GeV/n. Primary cosmic rays C (green) and O (red) flatten out at high energies followed by an increase in slope above a few hundred GeV/n. Nitrogen (orange) exhibits a spectral shape between the other two populations, evidencing its mixed primary and secondary sources.

It is important to recognize how the primary and secondary sources of GCR influence their spectral shapes and abundances, both for physics and modeling purposes. In the discussion that follows, we will group the ions according to primaries (C, O), secondaries (Li, Be, B), and a combination (N). The AMS data are compared to GCR models developed for space radiation applications that do not attempt to address GCR physics; however, it is informative to acknowledge that primary and secondary cosmic rays have fluxes with fundamentally different spectral shapes, which should be represented in the models. We will also compare AMS ion ratios to examine whether the GCR models reproduce the correct relative abundances and general trends between the spectral shapes.

3. Description of the Models

A short description of each of the models is included here to point out the major factors that determine each model's predicted spectral shape. Conceptually, GCR ions are produced at their cosmic sources and transported through the galaxy until they encounter the heliosphere. Their spectral shape at the edge of the heliosphere is called the Local Interstellar Spectrum (LIS). GCRs then enter the heliosphere and are modulated by the Sun's magnetic field and solar wind, which influences the lower energy part of the spectrum below tens of GeV/n. The models presented here empirically assume the shape of the LIS for each ion and then modulate the lower part of the spectrum using a single parameter called the modulation potential. The modulation potential, ϕ, was first introduced by Gleeson and Axford (1968), and is interpreted as the amount of energy lost by a particle as it travels through the heliosphere to Earth. The final spectral shape produced by each model at high energies depends on the form assumed for the LIS, while the spectral shape at low energies depends on both the LIS and the function used to modulate the spectrum.

3.1. BON2014 (NASA)

BON2014 (O'Neill et al., 2015) is a semi-empirical model that assumes an empirical LIS for each ion and then applies the physics of particle transport to produce GCR spectra at Earth. BON2014 is the only model of the three presented here that
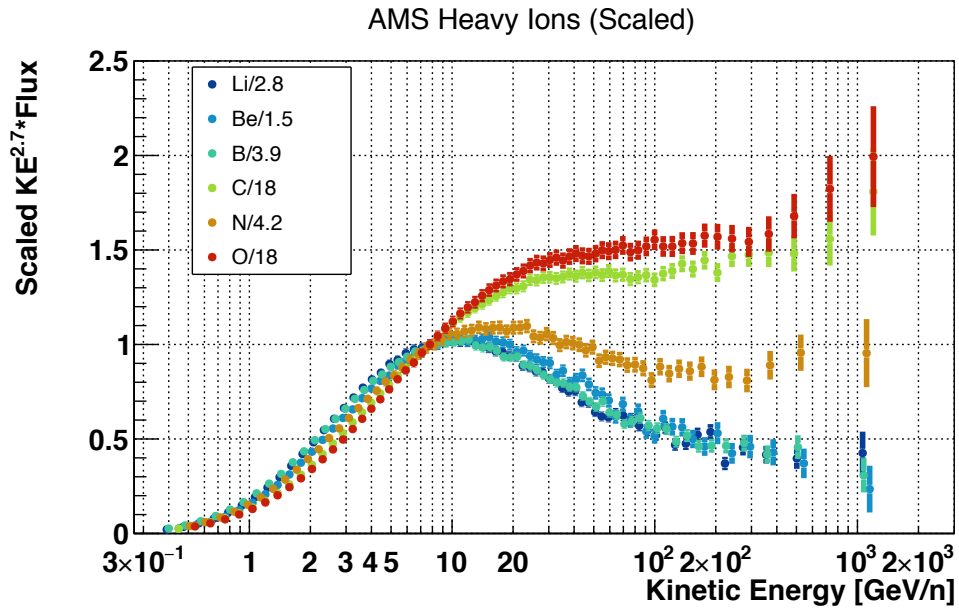
4

Figure 2: Spectra of heavy ions measured by AMS, rescaled by $KE^{2.7}$. An additional scaling factor, shown in the legend and equivalent to the flux ∼8 GeV/n, has been applied so that all fluxes could be compared on a similar scale. Li (dark blue), Be (blue), and B (turquoise) are secondary cosmic rays showing a characteristic downturn in the slope above ∼20 GeV/n. C (green) and O (red) are primary cosmic rays, showing a flattening of the spectrum followed by a possible increase in slope at high energies. N (orange) exhibits a spectrum that is a combination of primary and secondary sources.

solves the particle transport equation; the DLR and SINP models are both fully empirical.

BON2014 assumes an LIS spectrum, J_{LIS}, with the form:

$$J_{LIS} = j_{0,i}(E_N + E_0)^{\gamma_i}\beta_N^{-1}\beta^{\delta_i}(E + E_0)^{-\gamma_i} \tag{1}$$

where $j_{0,i}$, δ_i, and γ_i are free parameters for each GCR ion i, E is the kinetic energy per nucleon (KE/nuc) of the particle, E_0 is the proton rest energy, $\beta = v/c$, where v is the particle speed, c is the speed of light, and β_N is the relative velocity at E_N = 35 GeV/n (Golge et al., 2015). The specific parameters used for each ion can be found in O'Neill et al. (2015).

The modulation potential, ϕ, is derived from sunspot number (with an empirically-derived time lag applied) and then used to calculate the diffusion coefficient, κ:

$$\kappa = \frac{\kappa_0\beta R}{V_s\phi(t)}\left[1 + \left(\frac{r}{r_0}\right)^2\right] \tag{2}$$

where κ_0 is a normalization, R is rigidity, V_s is the solar wind speed, r is radius from the sun, and r_0 is a reference radius.

Finally, the diffusion coefficient is inserted into the GCR transport equation first proposed by Parker (1965). The modulation of the LIS is accomplished by solving the transport equation in 1D (therefore neglecting the Parker spiral), including the effects of convection with the solar wind, adiabatic cooling, and particle diffusion.

3.2. DLR Model

The DLR model developed by Matthia et al. (2013) is based on the International Organization for Standardization (ISO) GCR model by Nymmik et al. (1992, 1994, 1996) (ROSCOSMOS, ISO 15390:2004[1]). The DLR model retains the overall spectral shape and parameters derived for the ISO model with some modifications:

$$J_i(E,t) = \left[C_i\beta^{\alpha_i}R^{-\gamma_i}\right]\cdot\left[\left(\frac{R}{R + (0.37 + 3\cdot 10^{-4}\cdot W(t))^{1.45}}\right)^{b\cdot W(t)+c}\right]\frac{A_i}{|Z_i|}\frac{1}{\beta} \tag{3}$$

where $J_i(E,t)$ is the differential flux spectrum for each ion i, E is KE/nuc, t is time, R is rigidity, A_i is atomic number, Z_i is charge, and $\beta = v/c$. C_i, α_i, and γ_i retain the same values as used in the ISO model for each ion (Nymmik et al., 1992, 1994,

---

[1]https://www.iso.org/standard/37095.html

1996). The exponent $b \cdot W(t) + c$ is modified in the DLR model from that used in the ISO model.

The first factor in brackets represents the LIS and has a form similar to that used in BON2014. The second factor in brackets containing the parameter W controls the modulation of the spectrum. In the original ISO model, the modulation potential is represented by the term $(0.37 + 3 \cdot 10^{-4} \cdot W(t))^{1.45}$, where $W(t)$ is calculated from sunspot number with a time lag applied.

The DLR model treats the parameter W differently than the ISO model; rather than deriving it from sunspot number, W is treated as a rigidity-independent, free-parameter derived directly from cosmic ray measurements and neutron monitor (NM) counts. The values of $b = 0.02$ and $c = 4.7$ in the exponent were found by minimizing the absolute difference between the model and carbon GCR flux measured by the Cosmic Ray Isotope Spectrometer (CRIS) on the Advanced Composition Explorer (ACE) spacecraft. With these parameters defined, $W(t)$ is then derived by finding the best fit between the model and ACE data (or NM counts) at time t (Matthia et al., 2013).

3.3. SINP (ROSCOSMOS)

The new SINP model (Kuznetsov et al., 2017) is the simplest of the three models; however, it was developed with the feature to predict GCR spectra at Earth *and* distances from the sun greater than 1 AU. The SINP model uses different spectral shapes for GCR H and He then scales the He spectrum by a constant factor to produce spectra for all heavier ions up to Iron. The flux for H and He is given by:

$$J_{H,He}(E,t) = A_{H,He}E^{-\gamma} \left(\frac{E}{E + \phi_{H,He}(t)} \right)^{\Delta} \tag{4}$$

where E is KE/nuc, A is a normalization, $\Delta = 3.7$ and $\phi(t)$ is the modulation potential. For cases at 1 AU and beyond, $\phi(t)$ is given by:

$$\phi(t) = \begin{cases} \phi_0 + \kappa \cdot W(t - \Delta t) & \text{for } r = 1 \text{ AU} \\ \phi_0 r^{-\alpha} + \kappa(1 - r/120) \cdot W(t - \Delta t) & \text{for } r > 1 \text{ AU} \end{cases} \tag{5}$$

where W is the smoothed monthly sunspot number, Δt is a time lag of 15 months for odd solar cycles and 6 months for even solar cycles, r is distance from the Sun in AU, and $\alpha = 0.05$ for hydrogen and 0.07 for Helium (Kuznetsov et al., 2017). The model is calibrated with data to determine the values of A, γ, ϕ_0, and κ for H and He (Kuznetsov et al., 2017).

As mentioned above, the fluxes for all heavier ions ($Z = 3$ - 28) are given by scaling the Helium flux by a constant factor ζ_i: $J_i(E,t) = \zeta_i J_{He}$. In the SINP model,

all heavier ions are assumed to have the same spectral shape as helium, and no differentiation is made between primary or secondary GCR. For this reason, all ion ratios will simply be a straight line in energy or rigidity equal to the ratio of their constant factors.

4. Preparation of the Models and Data

Astroparticle experiments prefer to produce fluxes in units of particle rigidity (R), whereas the space radiation protection community prefers to work in units of particle kinetic energy (KE). In order to compare the GCR models to AMS measurements, it was necessary to convert them into the same units. In following with the space radiation community, the AMS fluxes for each of the individual heavy ions have been converted from units of rigidity to KE per nucleon, which are the native units of the BON2014, DLR, and SINP models.

Differential fluxes are converted from one set of units to the other via the following equation:

$$\frac{dF}{dT} = \frac{dF}{dR}\frac{dR}{dT} = \frac{T + E_0}{Z\sqrt{T(T + 2E_0)}} \frac{dF}{dR}. \tag{6}$$

where T is particle total kinetic energy, E_0 is the rest energy, R is rigidity, Z is the charge, $\frac{dF}{dT}$ is differential flux in units of total KE, $\frac{dF}{dR}$ is differential flux in units of rigidity. Equation 6 will convert flux in units of [GV m^2 s sr]$^{-1}$ to [GeV m^2 s sr]$^{-1}$. In order to obtain flux in units of KE per nucleon, $\frac{dF}{dT}$ is multiplied by the number of nucleons to give [GeV/n m^2 s sr]$^{-1}$. Further discussion of the flux and R to KE conversion is detailed in Section 2 of our previous paper (Norbury et al., 2018).

A subtlety of the calculation in Equation 6 is that some of the GCR ions have multiple stable isotopes that contribute to the measured flux. It is thus necessary to know the effective atomic mass number (dependent on the proportions of each isotope) to calculate the rest mass and number of nucleons. The atomic mass numbers used by the AMS collaboration and applied here are shown in Table 4.

To compare with the data, the models also required some post processing. Models produce fluxes for discrete energies, whereas particle detectors make measurements over a range of energies, defined by energy bins. As was done in our previous paper (Norbury et al., 2018), the discrete model flux values were interpolated using a cubic Lagrangian and then integrated across each energy bin defined by the AMS spectrum.

The ion ratios published by the AMS collaboration could not be converted into units of kinetic energy per nucleon - two ions with the same rigidity will have different kinetic energies per nucleon, thus the ratios aren't directly convertible from one set

Table 1: Atomic mass numbers calculated by the AMS collaboration to account for the isotopic composition of each GCR ion.

Ion	Atomic Mass Number	Reference
Li	6.5	Aguilar et al. (2018a)
Be	8.0	Aguilar et al. (2018a)
B	10.7	Aguilar et al. (2018a)
C	12	Aguilar et al. (2017)
N	14.5	Aguilar et al. (2018b)
O	16	Aguilar et al. (2017)

of units to the other. Instead, for the ion ratios only, the model flux for each ion was converted to units of rigidity [GV m^2 s sr]$^{-1}$ and then two were divided to generate the ion ratios in each AMS rigidity bin.

5. Comparison of Models with Measurements - Individual Ions

In the comparisons below, the AMS and model fluxes in units of kinetic energy per nucleon have been visualized on three separate scales to highlight different portions of the GCR spectrum. In Figures 3 - 8, the black circles correspond to AMS measurements and the BON2014 (blue), DLR (green), and SINP (red) models are plotted as histograms, indicating the width of each AMS energy bin. The top left plot shows the complete spectrum plotted on a log-log scale. The bottom left plot shows the ratio of the model flux divided by the AMS measurements across the complete AMS energy range. If the ratio is greater than 1, then the model overestimates the data. Likewise, if the ratio is less than 1, then the model underestimates the data. Two additional plots highlight the model-data comparison at low and high energies: at top right, the low energy part of the spectrum below 30 GeV/n is plotted on a linear-log scale; the bottom right plot emphasizes the high energy part of the spectrum by rescaling the data and model flux by (KE/n)$^{2.7}$.

At the end of this section, a quantitative comparison between the models and data will be shown using two statistics: absolute relative difference and normalized χ^2, as was done in our previous paper (Norbury et al., 2018). We note again that *energies between 0.25 - 4 GeV/n are estimated to be the most important for space radiation purposes.* In a study using BON2014 and HZETRN, Slaba and Blattnig (2014a) found that ions with $Z = 3 - 28$ contributed less than 0.1% of the total effective dose inside the human for energies < 250 MeV and only 5.1% for energies > 4 GeV/n behind 20 g/cm^2 of aluminum shielding. It should also be noted that these models were developed prior to the publication of this AMS data, before precision
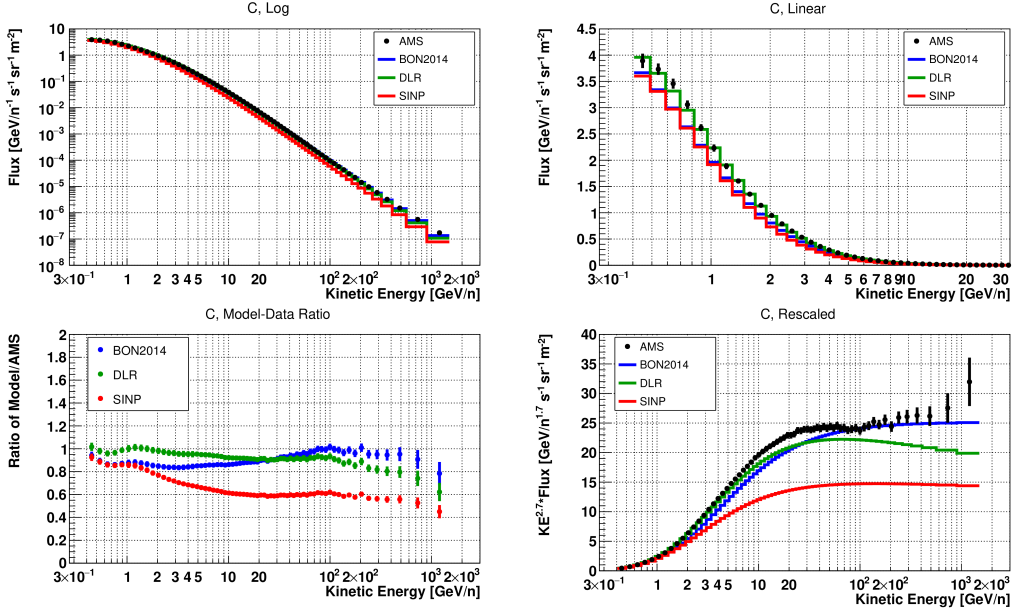
Figure 3: AMS carbon compared to models. AMS carbon measurements (black circles) are plotted alongside the BON2014 (blue), DLR (green) and SINP (red) models. The models are plotted as histograms to indicate the size of the energy bin corresponding the each AMS data point. **Top Left:** The complete carbon spectrum in log-log scale. **Bottom Left:** The model/data ratio for the complete spectrum. **Top Right:** The lower energy portion of the carbon spectrum in linear-log scale. **Bottom Right:** The carbon spectrum rescaled by $(KE/n)^{2.7}$ to emphasize the shape of the high energy part.

measurements of ions at high energies above a few tens of GeV/n were available.

5.1. Carbon Flux

Figure 3 shows the comparison between the three GCR models and AMS measurements of the primary GCR carbon. All of the models reproduce the spectrum fairly well below 1 GeV/n, as seen in the ratio (bottom right) and linear (top left) plots. The DLR (green) and BON2014 (blue) models underestimate the spectrum in places, but remain accurate to within 20% across almost the full spectrum. The SINP (red) model underestimates the flux by 20 - 40% for energies above ∼2 GeV/n. The rescaled (bottom right) plot shows that the DLR model reproduces the spectral shape well up to 100 GeV/n, but fails to turn up in slope as is observed in the data. BON2014 applies a constant flat slope above 100 GeV/n that approximately reproduces the observed spectral shape. SINP has a similar flattened spectral shape to BON2014 at high energies, but significantly underestimates the flux.
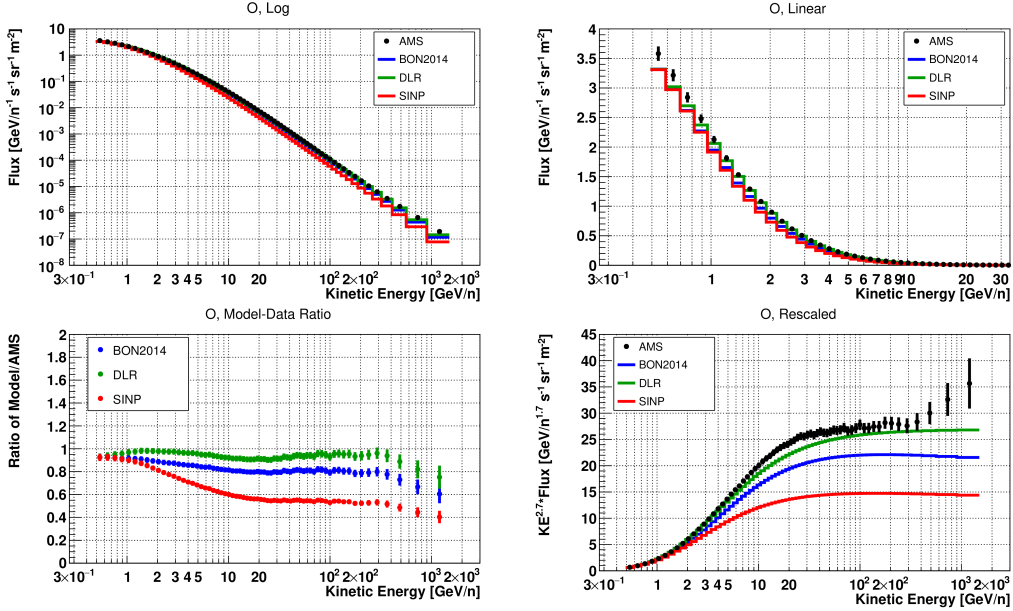
10

Figure 4: AMS oxygen compared to models as described in Figure 3.

5.2. Oxygen Flux

Figure 4 shows the comparison between the three GCR models and AMS measurements of the primary GCR oxygen. As seen in all the plots, the DLR model follows the data closely across the full energy range, reproducing the flux to within about 10%. BON2014 is accurate at low energies below a few GeV/n and shows a fairly accurate spectral shape overall, but underestimates the oxygen flux by 20% above 10 GeV/n. Again, the SINP model shows a similar spectral shape to the other two models, but underestimates the measurements by more than 40% above 10 GeV/n.

5.3. Nitrogen Flux

Figure 5 shows the comparison between the three GCR models and AMS measurements of GCR nitrogen, which is a combination of both primary and secondary sources. The DLR model does an excellent job reproducing this spectrum even at high energies, as seen in the bottom left plot. Both the DLR and BON2014 models show the characteristic downturn of the spectrum above ~20 GeV/n that is evidence of the secondary component in the spectrum. The SINP model, however, does not reflect the measured spectral shape. Helium is a primary GCR with a spectral shape
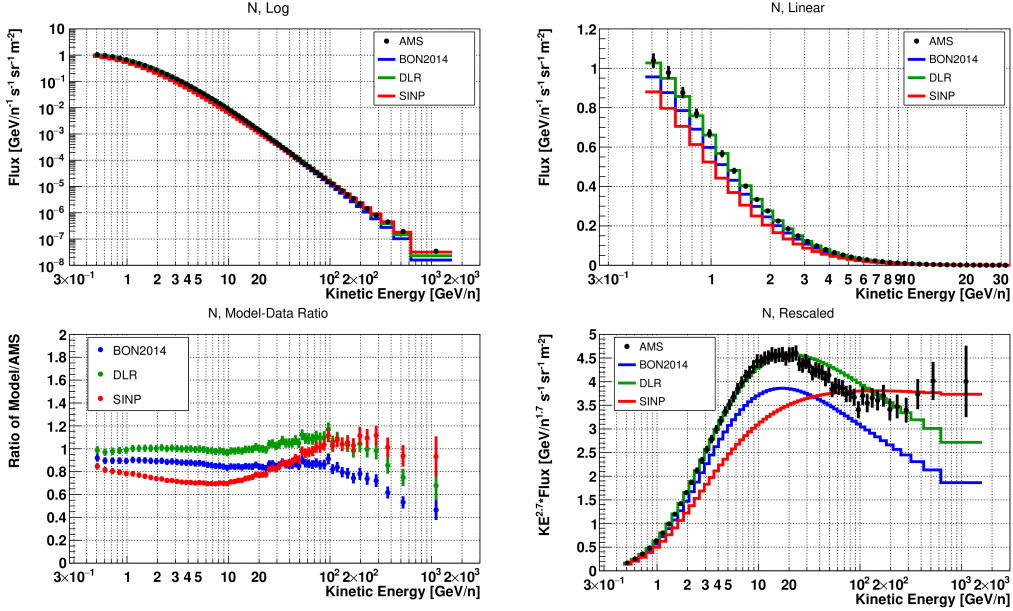
11

Figure 5: AMS nitrogen compared to models as described in Figure 3.

more similar to C and O. Here it becomes obvious that the SINP method to scale the He flux by a constant factor will not accurately reflect the spectral shape of GCR with secondary origins.

5.4. Lithium Flux

Figure 6 shows the comparison between the three GCR models and AMS measurements of the secondary GCR lithium. In all of the plots, it can be observed that none of the models reproduce the lithium measurements. Each model underestimates the data below 20 GeV/n, while SINP and the DLR models significantly overestimate the flux at high energies. BON2014 has a reasonable spectral shape, but the normalization is too low. Neither SINP or DLR produce a realistic spectral shape. Generating the Li spectrum has clearly been a challenge for all models and the new AMS measurements should lead to significant improvement in the future.

5.5. Beryllium Flux

Figure 7 shows the comparison between the three GCR models and AMS measurements of the secondary GCR beryllium. In this case, BON2014 follows the data very well up to 20 GeV/n, differing by only $\sim \pm 10\%$. The DLR model matches well below 2 GeV/n, but then systematically underestimates the measurements by
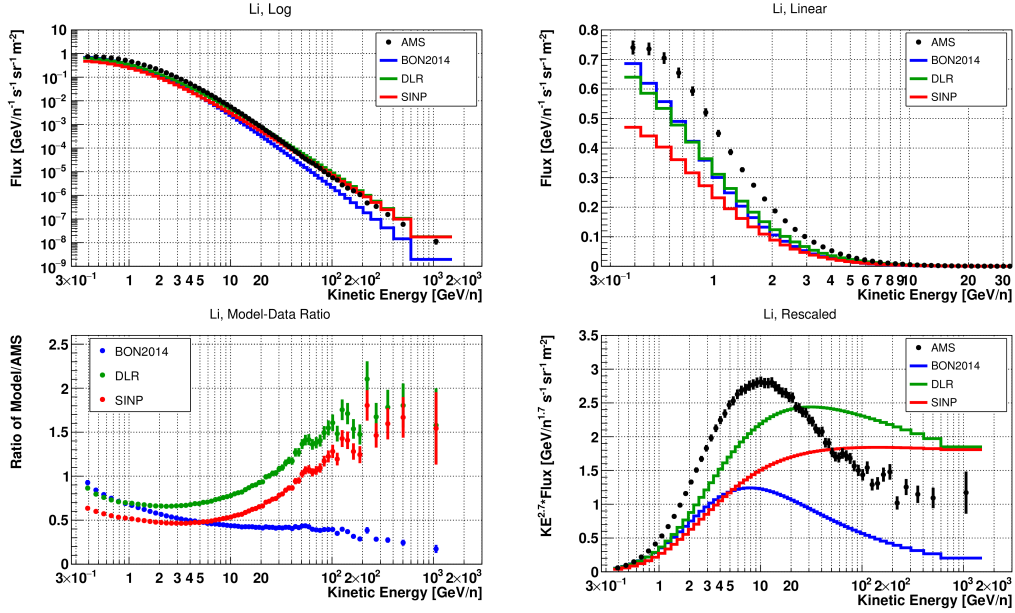
12

Figure 6: AMS lithium compared to models as described in Figure 3.
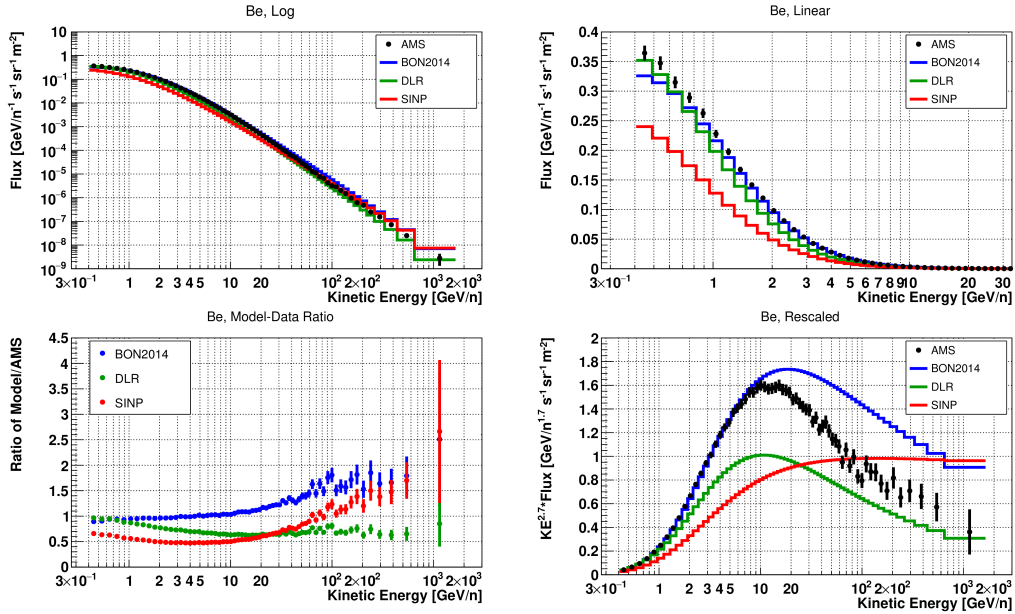

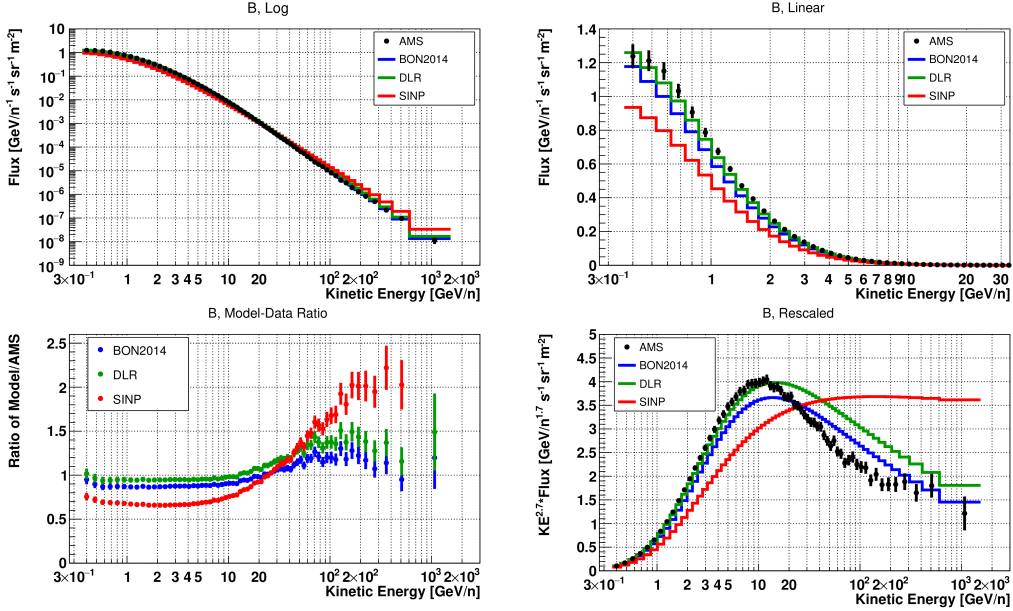Figure 7: AMS beryllium compared to models as described in Figure 3.

Figure 8: AMS boron compared to models as described in Figure 3.

as much as 45%. Both BON2014 and the DLR model attempt to reproduce the characteristic downturn in the spectrum. Once again, the SINP model produces an incorrect spectral shape and underestimates the spectrum up to 100 GeV/n where it crosses the data and then overestimates the flux.

5.6. Boron Flux

Figure 8 shows the comparison between the three GCR models and AMS measurements of the secondary GCR boron. For boron, the DLR and BON2014 models follow the data closely up to ∼10 GeV/n and then both attempt to reproduce the changing slope of the spectrum. They do fairly well, but the slope is steeper in the actual measurements. Again, the SINP model's primary spectral shape does not match the data well, underestimating the measurements at lower energies and overestimating the measurements above 20 GeV/n.

5.7. Quantitative Comparison

The models were compared against the data using two different numerical measures, the absolute relative difference, as done in previous studies by O'Neill et al. (2015) and Slaba et al. (2014), and a normalized χ^2 statistic similar to an assessment of GCR models carried out in Mrigakshi et al. (2012). A series of detailed studies

14

investigating GCR environmental models (Slaba and Blattnig, 2014a,b; Slaba et al., 2014) identified three energy ranges (< 1.5, 1.5 - 4.0 , and > 4.0 GeV/n) with particular importance in the context of space radiation protection, making them suitable ranges to use for quantitative comparisons. An intermediate interval from 4 - 20 GeV/n is added to discriminate between models that match GCR spectra fairly well in that energy range despite deviating significantly at the high or low end. Lastly, the models were compared across the full spectrum to identify which best reproduced the AMS data overall.

The two statistics were calculated for five different energy ranges and tabulated in Tables 5.7 and 5.7, respectively.

The absolute relative difference is given by:

$$|Rd| = \frac{1}{N} \sum_{i=1}^{N-1} \frac{|F_{model,i} - F_{data,i}|}{F_{data,i}} \tag{7}$$

where N is the total number of energy bins and $F_{model,i}$ and $F_{data,i}$ are the flux in energy bin i for model and data, respectively. This sum can also be understood as the average percent difference (when multiplied by 100%) between model and data across the energy range. Table 5.7 lists $|Rd|$ in percent (%) for each model. The lowest values are highlighted in red, indicating the model that best represents the data in each energy range.

It is also useful to consider a normalized χ^2 statistic (χ^2/NDF), which incorporates uncertainties on the data:

$$\chi^2/NDF = \frac{1}{N} \sum_{i=1}^{N} \frac{(F_{model,i} - F_{data,i})^2}{\sigma_i^2} \tag{8}$$

where $F_{model,i}$, $F_{data,i}$, and i are the same as Equation 7 and σ_i is the uncertainty on the data in bin i. N is the number of energy bins. The χ^2/NDF values are tabulated in Table 5.7 and the lowest values are highlighted in red.

Overall, the DLR model best-reproduces the AMS data compared to BON2014 and SINP. In the cases of C, O, and N, the DLR model differs from data by less than 10% in all energy ranges in Table 5.7. The DLR model also does an excellent job matching the AMS B measurements up to 20 GeV/n. For Li, the DLR model has the best results, but differs significantly from data by 22 - 32%. BON2014 is the best performer for Be, reproducing the spectrum up to 20 GeV/n with less than 7% difference from data.

Lower values of normalized χ^2 indicate a better match between models and data and a value of 1.0 or less indicates that the models are within the data error bars.

Table 2: Absolute relative difference ($|Rd|$) in percent (%) between AMS data and the integrated flux calculated from models in selected energy ranges. The lowest values are highlighted in red.

$|Rd|$ in % for Selected Energy Ranges (GeV/n)				
Model	**< 1.5**	**1.5 - 4**	**> 4**	**4 - 20**	**Full Spectrum**
Primaries					
Carbon					
SINP	13	26	40	38	35
DLR	**1.8**	**3.0**	10	**7.1**	**8.2**
BON2014	12	16	**8.3**	13	9.6
Oxygen					
SINP	9.5	22	44	39	37
DLR	**4.3**	**2.7**	**7.4**	**7.2**	**6.5**
BON2014	8.1	12	20	18	18
Combination					
Nitrogen					
SINP	21	28	16	28	18
DLR	**1.3**	**0.34**	**5.3**	**1.4**	**4.2**
BON2014	10	11	17	15	16
Secondaries					
Lithium					
SINP	45	53	34	46	38
DLR	27	**34**	**33**	**22**	**32**
BON2014	**26**	45	60	55	53
Beryllium					
SINP	41	51	36	48	39
DLR	9.9	25	**33**	35	29
BON2014	**6.6**	**2.7**	34	**5.3**	**27**
Boron					
SINP	31	34	43	24	40
DLR	**4.8**	**5.2**	19	**3.9**	16
BON2014	12	13	**12**	8.8	**12**

Table 3: Normalized χ^2 for each model compared to AMS data in selected energy ranges. The lowest values are highlighted in red.

χ^2/NDF for Selected Energy Ranges (GeV/n)					
Model	< 1.5	1.5 - 4	> 4	4 - 20	Full Spectrum
Primaries					
Carbon					
SINP	23.3	90.5	214	254	175
DLR	**0.653**	**1.49**	**10.9**	**9.44**	**8.45**
BON2014	18.0	31.3	14.6	32.6	17.2
Oxygen					
SINP	11.2	71.0	182	198	149
DLR	**2.21**	**1.02**	**5.37**	**7.17**	**4.46**
BON2014	7.72	20.9	36.7	43.2	31.6
Combination					
Nitrogen					
SINP	41.6	76.9	33.5	77.2	39.8
DLR	**0.226**	**0.020**	**1.68**	**0.264**	**1.30**
BON2014	9.62	13.0	15.5	20.4	14.5
Secondaries					
Lithium					
SINP	278	401	129	290	181
DLR	**102**	**162**	**60.4**	**73.9**	**78.2**
BON2014	108	295	273	407	253
Beryllium					
SINP	184	335	120	278	156
DLR	14.0	82.8	78.6	143	71.5
BON2014	**4.75**	**1.14**	**34.4**	**4.70**	**26.4**
Boron					
SINP	72.8	174	91.5	102	98.8
DLR	**1.90**	**4.07**	23.3	**2.79**	18.2
BON2014	11.5	25.0	**11.1**	14.6	**12.8**

Table 5.7 shows that the DLR model has comparatively low χ^2/NDF values with multiple instances of values near or less than 1. In particular, the DLR model falls almost completely within the error bars for nitrogen up to ∼20 GeV/n.

6. Comparison of Models with Measurements - Ion Ratios

Ion ratios provide important information useful in GCR modeling regarding the relative spectral shapes and abundances between ion species. These new high-precision AMS measurements are an opportunity to test the current state of the models considered here and inform potential improvements in the future.

As mentioned in Section 3.3, the SINP model predicts a constant value across the rigidity spectrum equivalent to the ratio of the ions' scaling factors. SINP cannot reproduce rigidity-dependent changes in spectral shape between two ions, thus a good prediction from SINP would be a value similar to the average ion ratio across the spectrum or in the rigidity range of interest for space radiation.

6.1. Primary-to-Primary

The AMS carbon-to-oxygen (C/O) ratio, shown as black circles in Figure 9 (top), has a slight negative slope, but the ion ratio changes by a total of only ∼ 20% across the spectrum. Indeed, the SINP model (red) predicts a constant ratio of ∼1, and in this case, is a fairly consistent representation of the data, as seen in the model-to-data ratio plot in Figure 9 (bottom). The DLR model (green) captures the relationship between C and O extremely well up to 200 GV, while BON2014 (blue) predicts a slope in the wrong direction.

6.2. Secondary-to-Primary

AMS comparisons of secondary (Li, Be, B) ions to primary (C, O) ions, shown as black circles in Figures 10 - 12 (top), all show a characteristic "S" shape with an increase in slope at low rigidities followed by a strongly decreasing slope across the middle rigidity range and a flattening at high rigidities.

The model predictions for Li/C and Li/O in Figure 10 (left and right, respectively) are poor. This is not surprising as none of the models accurately reproduced the Li spectrum, as discussed in Section 5.4.

Performance is better for Be/C and Be/O in Figure 11 (left and right, respectively). BON2014 (blue) overpredicts while DLR (green) underpredicts, but both models produce slopes across the spectrum similar to the data.

Figure 12 shows more accurate model results for the B/C (left) and B/O (right) ratios. BON2014 (blue) and the DLR model (green) both follow the overall shapes
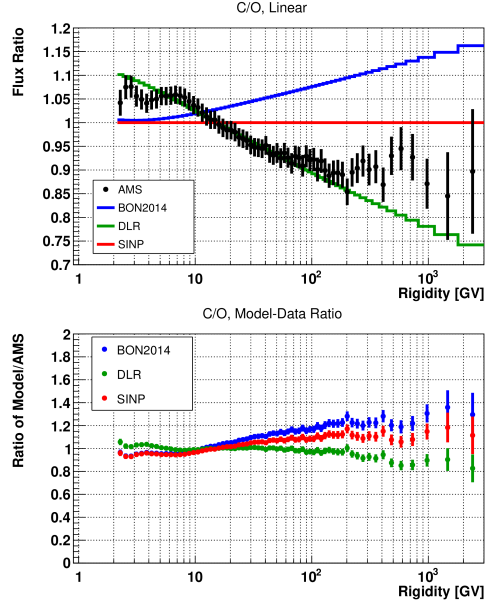
Figure 9: **Top:** AMS primary carbon flux divided by primary oxygen fluxes (C/O) (black circles) compared to GCR models BON2014 (blue), DLR (green), and SINP (red). **Bottom:** Model-data ratio.
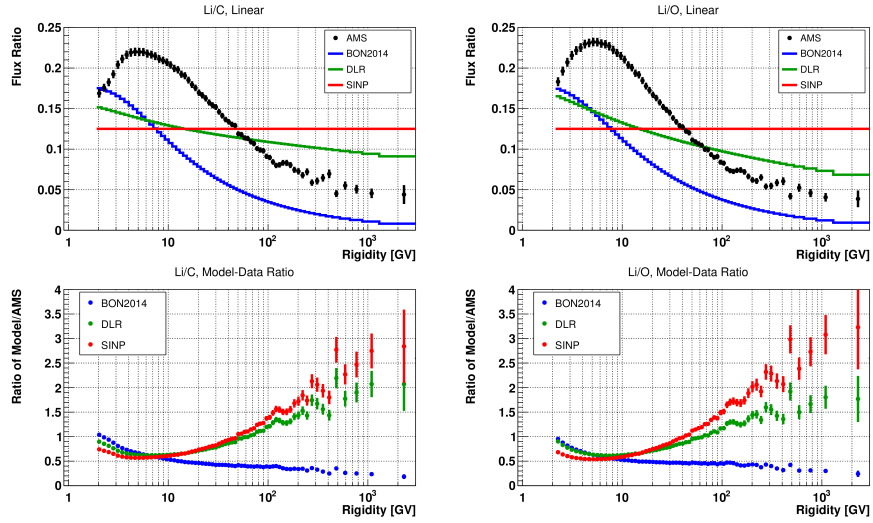

Figure 10: AMS secondary ion fluxes divided by primary ion fluxes compared to models. **Left:** Li/C (top) with model-data ratio (bottom). **Right:** Li/O (top) with model-data ratio (bottom).
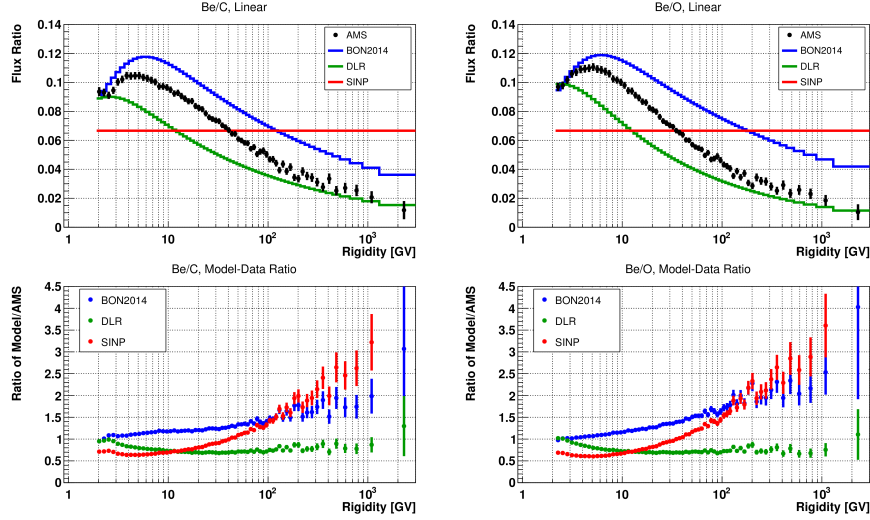
19

Figure 11: AMS secondary ion fluxes divided by primary ion fluxes compared to models. **Left:** Be/C (top) with model-data ratio (bottom). **Right:** Be/O (top) with model-data ratio (bottom).

of the ratios very well. The SINP constant values are high compared to the overall spectrum, but are closer to data for the rigidity range of interest to space radiation.

6.3. Secondary-to-Secondary

Figure 13 shows the AMS flux ratios (black circles) between secondary GCRs Li/B (left panels) and Be/B (right panels). The ion ratios are nearly consistent with straight lines across the rigidity range. Indeed, the SINP model's straight line prediction works well to reproduce the overall behavior of each ratio, but has lower relative abundances between Li and Be to B compared to data. Both BON2014 and the DLR model have incorrect shapes for Li/B. BON2014 produces a more correct shape for Be/B, but overestimates the increasing slope towards higher rigidities.

6.4. Combination-to-Primary and -Secondary

Figure 14 shows AMS nitrogen compared to the primary oxygen (N/O) (black circles, left panels) and nitrogen compared to the secondary boron (N/B) (black circles, right panels). The nitrogen spectrum reflects a combination of primary and secondary sources, so N/O shows the characteristic "S" shape seen when comparing secondary-to-primary GCR due to nitrogen's secondary component. The N/B ratio rises more steeply across the spectrum than seen in the secondary-to-secondary ratios due to the presence of nitrogen's primary component.
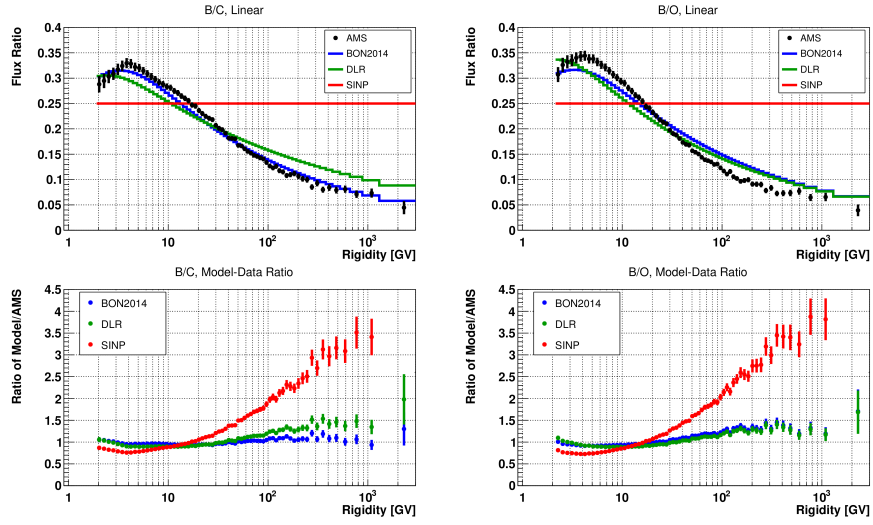
20

Figure 12: AMS secondary ion fluxes divided by primary ion fluxes compared to models. **Left:** B/C (top) with model-data ratio (bottom). **Right:** B/O (top) with model-data ratio (bottom).
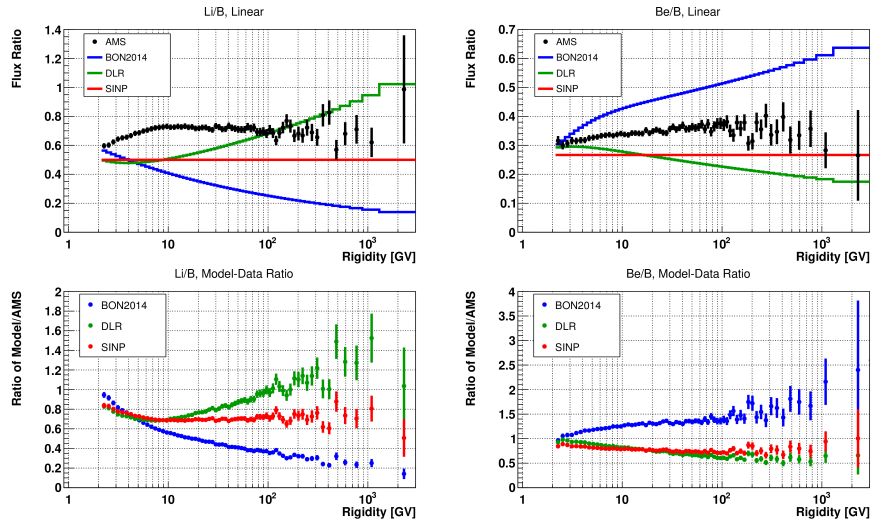

Figure 13: AMS secondary ion fluxes divided by secondary ion fluxes compared to models. **Left:** Li/B (top) with model-data ratio (bottom). **Right:** Be/B (top) with model-data ratio (bottom).
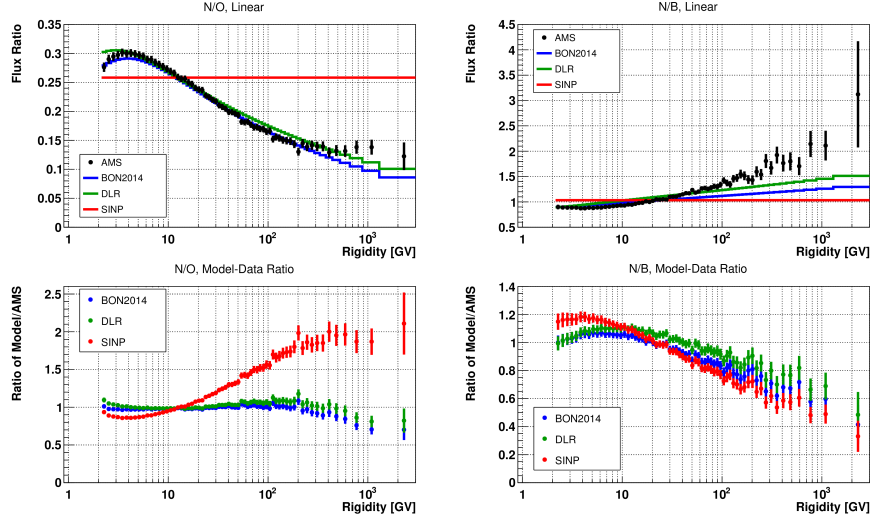
Figure 14: AMS nitrogen divided by primary oxygen flux (N/O) (left panels) and secondary boron flux (N/B) (right panels) compared to models.

Both BON2014 and the DLR model reproduce the N/O ratio very well (Figure 14 left), within 10% of the data across most of the rigidity range. The match between models and data for N/B below 20 GV is fairly good, however neither BON2014 nor the DLR model increase steeply enough at high rigidities.

6.5. Quantitative Comparison

The relative difference $|Rd|$ and normalized χ^2 were calculated between the AMS ratio measurements and the results from each model, compiled in Table 6.5. In this case, only the full rigidity range was considered. The DLR model showed the best performance in reproducing the ion ratio measurements overall, which is unsurprising considering it also performed very well in reproducing the individual ion fluxes. BON2014 best-reproduced B/C and B/O by a small margin and SINP performed best for Be/B, which was close to a constant ratio across all rigidities.

7. Discussion

The new high-precision, high-resolution heavy ion measurements from AMS (Aguilar et al., 2017, 2018a,b) provide an excellent independent data set with which to compare current GCR models used in space radiation protection applications. Furthermore, these recently published AMS fluxes of Li, Be, B, C, N, and O provide an

22

Table 4: Absolute relative difference ($|Rd|$) in percent (%) and normalized χ^2 between the model ratio and AMS ratio measurements across the full spectrum in rigidity. The lowest values are highlighted in red.

Ion Ratio	$|Rd|$ in %			χ^2/NDF		
	SINP	**DLR**	**BON2014**	**SINP**	**DLR**	**BON2014**
Primary-to-Primary						
C/O	7.0	**2.9**	12	7.75	**1.26**	23.5
Secondary-to-Primary						
Li/C	47	**33**	53	165	**111**	306
Li/O	55	**30**	50	204	**102**	270
Be/C	51	**24**	37	102	67	**64**
Be/O	61	**25**	54	130	**64**	125
B/C	71	17	**5.6**	304	19	**3.2**
B/O	86	**14**	16	401	**14**	17
Secondary-to-Secondary						
Li/B	29	**19**	53	75	**50**	205
Be/B	**22**	28	38	**35**	42	62
Combination-to-Primary						
N/O	39	4.4	**3.9**	121	2.0	**1.2**
Combination-to-Secondary						
N/B	20	**10**	13	19	**6.4**	7.9

Statistic across Full Spectrum (GV)

exciting opportunity to improve the models' spectral shapes across a broad energy range. The AMS measurements show that GCR from primary, secondary, or a combination of astrophysical sources result in different spectral shapes and ion ratios, particularly at high energies. Both BON2014 and the DLR model produce different spectral shapes for each ion, allowing them to make a distinction between the two populations of GCR sources. The SINP model assumes the same spectral shape for helium and all heavier ions, imposing a primary-like spectral shape for all ions.

The DLR model shows the best performance in reproducing the AMS measurements overall for the individual fluxes and the ion ratios. BON2014 also performs well, particularly in the energy ranges of interest for space radiation. None of the models were able to produce a correct spectral shapes for Li. Referring to Table 5.7, BON2014 and the DLR model generally differ from data by less than 20% for energies up to 20 GeV/n. In most cases, the absolute relative difference is closer to 10% indicating that these models reproduce the GCR environment very well.

References

Aguilar, M., et al., 2017. Observation of the identical rigidity dependence of He, C, and O cosmic rays at high rigidities by the Alpha Magnetic Spectrometer on the International Space Station. Physical Review Letters 119, 251101. doi:`10.1103/PhysRevLett.119.251101`.

Aguilar, M., et al., 2018a. Observation of new properties of secondary cosmic rays lithium, beryllium, and boron by the Alpha Magnetic Spectrometer on the International Space Station. Physical Review Letters 120, 021101. doi:`10.1103/PhysRevLett.120.021101`.

Aguilar, M., et al., 2018b. Precision measurement of cosmic-ray nitrogen and its primary and secondary components with the Alpha Magnetic Spectrometer on the International Space Station. Physical Review Letters 121, 051103. doi:`10.1103/PhysRevLett.121.051103`.

Gleeson, L.J., Axford, W.I., 1968. Solar modulation of galactic cosmic rays. The Astrophysical Journal 154, 1011–1026. doi:`10.1086/149822`.

Golge, S., O'Neill, P.M., Slaba, T.C., 2015. NASA galactic cosmic radiation environment model: Badhwar - O'Neill (2014). Proceedings of Science: The 34th International Cosmic Ray Conference 80. 30 July - 6 August, 2015, The Hague, The Netherlands.

Henry, R.B.C., Edmunds, M.G., Kppen, J., 2000. On the cosmic origins of carbon and nitrogen. The Astrophysical Journal 541, 660–674. doi:`10.1086/309471`.

Kuznetsov, N., Popova, H., Panasyuk, M., 2017. Empirical model of long-time variations of galactic cosmic ray particle fluxes. Journal of Geophysical Research: Space Physics 115, 1463–1472. doi:`10.1002/2016JA022920`.

Matthia, D., Thomas Berger, T., Mrigakshi, A., Reitz, G., 2013. A ready-to-use galactic cosmic ray model. Advances in Space Research 51, 329–338. doi:`10.1016/j.asr.2012.09.022`.

Mrigakshi, A.I., Matthia, D., Berger, T., Reitz, G., 2012. Assessment of galactic cosmic ray models. Journal of Geophysical Research: Space Physics 117. doi:`10.1029/2012JA017611`.

Norbury, J., Whitman, K., Lee, K., Slaba, T., Badavi, F., 2018. Comparison of space radiation GCR models to recent AMS data. Life Sciences in Space Research 18, 64–71. doi:`10.1016/j.lssr.2018.05.003`.

Nymmik, R., Panasyuk, M., Pervaya, T., Suslov, A., 1992. A model of galactic cosmic ray fluxes. International Journal of Radiation Applications and Instrumentation. Part D. Nuclear Tracks and Radiation Measurements 20, 427–429. doi:`10.1016/1359-0189(92)90028-T`.

Nymmik, R., Panasyuk, M., Pervaya, T., Suslov, A., 1994. An analytical model describing dynamics of galactic cosmic ray heavy particles. Advances in Space Research 14, 759–763. doi:`10.1016/0273-1177(94)90538-X`.

Nymmik, R., Panasyuk, M., Suslov, A., 1996. Galactic cosmic ray flux simulation and prediction. Advances in Space Research 17, 19–30. doi:`10.1016/0273-1177(95)00508-C`.

O'Neill, P., Golge, S., Slaba, T., 2015. Badhwar - O'Neill 2014 galactic cosmic ray flux model description. NASA Technical Paper 2015-218569.

Parker, E.N., 1965. The passage of energetic charged particles through interplanetary space. Planetary Space Science 13, 9. doi:`10.1016/0032-0633(65)90131-5`.

Slaba, T., Blattnig, S., 2014a. GCR environmental models I: Sensitivity analysis for GCR environments. Space Weather 12, 217–224. doi:`10.1002/2013SW001025`.

Slaba, T., Blattnig, S., 2014b. GCR environmental models II: Uncertainty propagation methods for GCR environments. Space Weather 12, 225–232. doi:`10.1002/2013SW001026`.

Slaba, T., Xu, X., Blattnig, S., Norman, R., 2014. GCR environmental models III: GCR model validation and propagated uncertainties in effective dose. Space Weather 12, 233–245. doi:`10.1002/2013SW001027`.

Strong, A.W., Moskalenko, I.V., Ptuskin, V.S., 2007. Cosmic-ray propagation and interactions in the Galaxy. Annual Review of Nuclear and Particle Science 57, 285–327. doi:`10.1146/annurev.nucl.57.090506.123011`.

Vangioni-Flam, E., Cass, M., Audouze, J., 2000. Lithium-beryllium-boron: origin and evolution. Physics Reports 333, 365–387. doi:`10.1007/s11207-016-1014-y`.